Interdecadal Change of the Structure of the ENSO Mode and Its Impact on the ENSO Frequency*

SOON-IL AN AND BIN WANG

International Pacific Research Center,+ School of Ocean and Earth Science and Technology, University of Hawaii at Manoa, Honolulu, Hawaii

(Manuscript received 23 April 1999, in final form 17 August 1999)

ABSTRACT

In the late 1970s, the ENSO cycle exhibited frequency change. The oscillation period increased from 2–4 yr (high frequency) during 1962–75 to 4–6 yr (low frequency) during 1980–93. Observations suggest that this frequency change was accompanied by a significant change in the structure of the coupled ENSO mode. In comparison with the high-frequency regime, the structure of the coupled mode in the low-frequency regime shows three distinctive features during the warm phase of ENSO: the eastward shift of the westerly anomalies, the meridional expansion of the westerly anomalies, and the weaker intensity of the easterly anomalies in the eastern Pacific.

To test the robustness of the relationship between the oscillation period and the structure of the coupled mode, the authors designed empirical atmospheric models based on observations and coupled them with the ocean model of Zebiak and Cane. Numerical experiments demonstrate that the ENSO period is sensitive to changes in the wind anomaly pattern in a way much like the observed ENSO frequency–structure relation. The increase of the ENSO period after 1980 is mainly due to the eastward shift of the zonal wind stress with respect to the SST anomalies. Physical explanations of the dependence of ENSO frequency on the structure of the coupled mode are provided by diagnosing the relative contributions of the thermocline feedback and zonal advection feedback on ENSO evolution.

1. Introduction

In recent years understanding of the physics of the El Niño–Southern Oscillation (ENSO) has rapidly improved as a result of great efforts by many researchers and owing to an accumulation of and improvement in observations. Relatively reliable Comprehensive Ocean–Atmosphere Data Set surface winds and sea surface temperature (SST) data extend back to the 1960s. They are useful for detecting decadal variations of ENSO cycles.

The interdecadal climate shift in the late 1970s exhibits global-scale variations in sea surface temperature, upper-ocean heat content, and winds in the Pacific and Atlantic oceans (Nitta and Yamada 1989; Kushnir 1994; Trenberth and Hurrel 1994; Latif and Barnett 1994; Zhang and Levitus 1997). Moreover, the climate shift had a significant impact on ENSO onset (Wang 1995) and prediction skills of the coupled ocean–atmosphere models (Balmaseda et al. 1995; Kirtman and Schopf 1998). A number of hypotheses have been recently proposed to explain the origin of the decadal variability in ENSO behavior (Gu and Philander 1997; Zhang et al. 1998; Wang et al. 1999a; Barnett et al. 1999). The precise processes determining the interdecadal variations of ENSO behavior remains controversial.

In comparison with the ENSO timescale, the interdecadal variation may be considered as a slowly evolving mean state upon which ENSO evolves. Previous ENSO studies (e.g., Battisti and Hirst 1989; Wakata and Sarachik 1991; Wang and Fang 1996; Kirtman and Schopf 1998) have recognized that the mean state tends to influence ENSO characteristics including the period, amplitude, and phase locking to the annual cycle. Such changes in ENSO characteristics may result not only from a direct impact by the mean state change but also from indirect influences of the changes in coupling processes, including the degrees of the coupling and changes in anomalous atmospheric or oceanic responses. Although the dependence of the frequency and growth rate

* SOEST Contribution Number 4876 and IPRC Contribution Number IPRC-19.

+ The International Pacific Research Center is partly sponsored by Frontier Research System for Global Change.

Corresponding author address: Dr. Soon-Il An, International Pacific Research Center, SOEST, University of Hawaii at Manoa, Honolulu, HI 96822.
E-mail: sian@soest.hawaii.edu

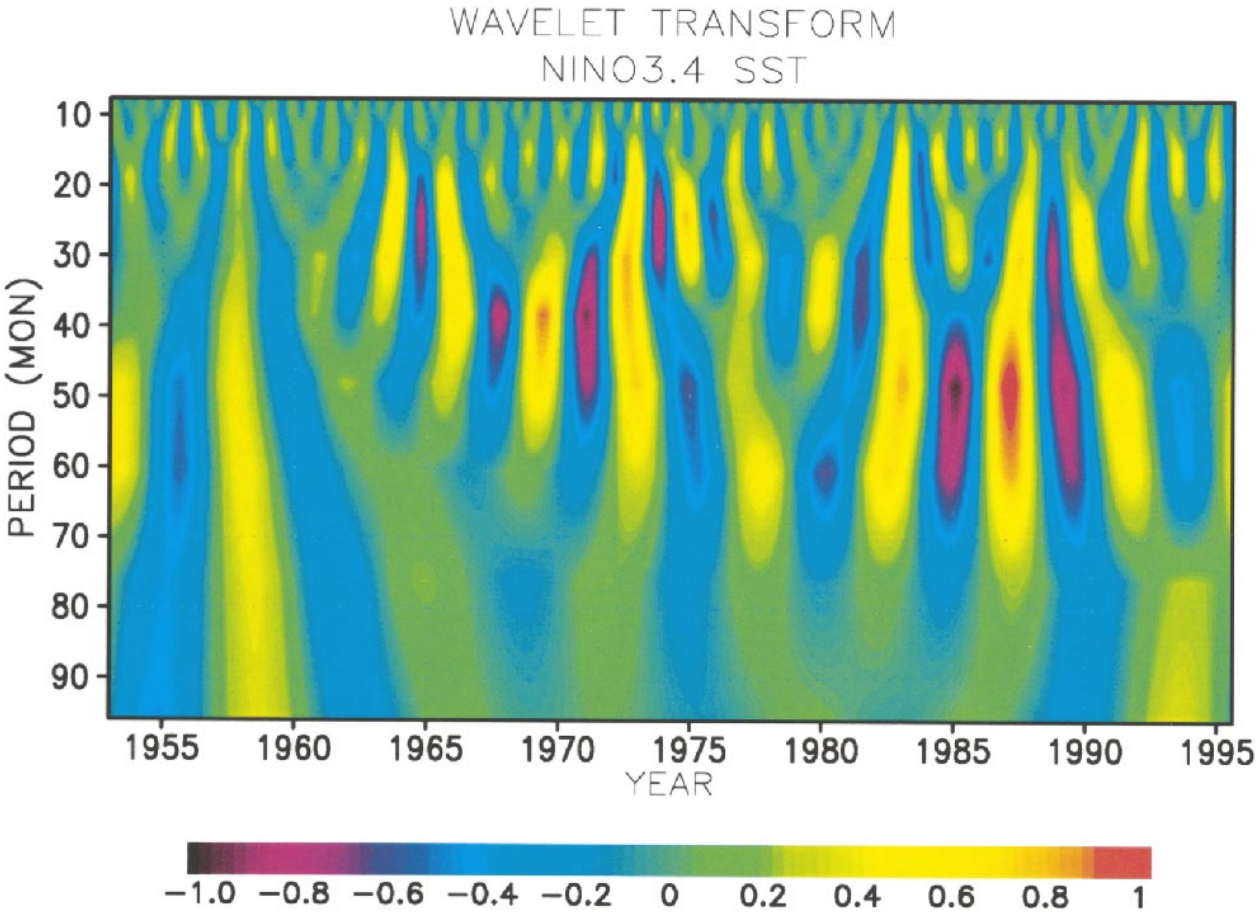

FIG. 1. The real part of the wavelet analysis of the Niño-3.4 SST anomaly, which shows the variance as a function of oscillation period and time.

of the coupled mode on coupling coefficients has been well known (Hirst 1986, 1988; Wakata and Sarachik 1991; Jin and Neelin 1993), the relationship between the structure of the dominant ENSO mode and the frequency and amplitude of ENSO has not been investigated.

In the present study, we will first document, using observed data, distinctive patterns of the wind and SST anomalies that appeared during periods with different dominant ENSO frequencies (section 2). We will then use intermediate coupled models to show that the structure of the ENSO mode determines its oscillation period (section 3). In section 4, we further explore the frequency changes due to changes in the horizontal structure of the coupled mode using idealized intermediate coupled models. A dynamical interpretation of the results is provided in section 5. The last section presents a summary and a discussion.

2. Distinct structures of the coupled mode in low- and high-frequency ENSO regimes

In order to reveal changes of ENSO frequency, we apply a wavelet analysis to a representative ENSO index, that is, the time series of the Niño-3.4 SST anomaly (the SST anomalies averaged over the area 5°S–5°N, 170°–120°W), which is obtained from the National Center for Environmental Prediction (NCEP) (Ji et al. 1995). The wavelet analysis has been applied to the climate data (e.g., Meyers et al. 1993; Lau and Weng 1995; Wang and Wang 1996) and provides a useful tool to reveal frequency localization in climate signals. The real part of the wavelet transform of the ENSO index is shown in Fig. 1. The frequency of ENSO changes with time. For instance, a period of 20–30 months dominates during 1962–67 while a period of 30–50 months dominates during 1967–73. From 1980 to the early 1990s an even longer period of 40–60 months is dominant. An evident change of frequency of ENSO cycle (from a relatively high to a relatively low frequency) occurs in the late 1970s, which concurs with the prominent climate shift in the North Pacific (Nitta and Yamada 1989; Trenberth 1990). It appears that the interdecadal change of Pacific climate not only affected the onset process of the ENSO (Wang 1995), but also affected the frequency of ENSO events. In the following we compare the two frequency regimes by focusing on the structure of the coupled ENSO mode.

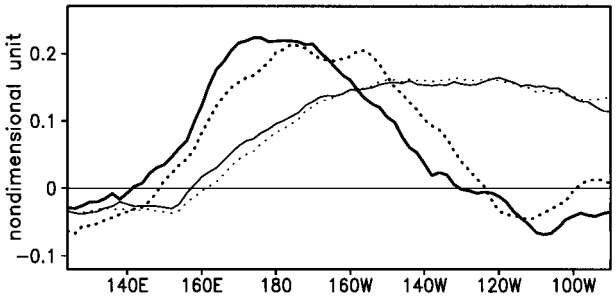

FIG. 2. First SVD mode between the tropical zonal wind stress anomaly (heavy line) and SST anomaly (thin line) calculated for the two periods Jan 1962–Dec 1973, and Jan 1981–Dec 1992, which are associated with different oscillation frequency regimes. The SVD modes for the former and latter periods are indicated by solid and dotted lines, respectively.

To explore possible change in the horizontal structure of the coupled mode, we compare the structure of the zonal wind stress and SST anomalies during the two decades of 1962–73 and 1981–92 using the method of singular value decomposition (SVD) (Bretherton et al. 1992). The SST (T) and zonal wind stress (τ_x) anomalies are decomposed in terms of their eigenvectors, $e_n(x, y)$ and $f_m(x, y)$, that is,

$$T(x, y, t) = \sum_n \alpha_n(t) e_n(x, y) \quad (1)$$

$$\tau_x(x, y, t) = \sum_m \beta_m(t) f_m(x, y), \quad (2)$$

where α_n and β_m denote the time coefficient associated with SST and wind stress anomalies, respectively. They are calculated by projecting SST and wind stress anomaly fields at a given time on each eigenvector. The SVD helps to identify coupled modes by maximizing the correlation between $\alpha_n(t)$ and $\beta_m(t)$ (Bretherton et al. 1992). Before applying the SVD method, each variable is averaged over the latitude band between 5°S and 5°N, because the strongest interannual variation in the Pacific is confined to this region. Data used here are the Florida State University (FSU) wind stress data (Goldenberg and O'Brien 1981) and the NCEP reconstructed SST data (Reynolds and Smith 1994). It might be considered that those two datasets are qualified for the interdecadal variability study, because their relative homogeneity and objectivity resulted from the application of the optimal reanalysis method (Kubota and O'Brien 1988; Smith et al. 1994; Reynolds and Smith 1995; Shriver and O'Brien 1995; Wang 1995; S. R. Smith et al. 1996; T. M. Smith et al. 1996b).

The first SVD mode is shown in Fig. 2, which explains 99% (for the first decade) and 98% (for the second decade) of the total covariance between wind stress and SST anomalies. The SST patterns that appeared during the two decades are very similar. However, the maximum zonal wind stress during 1962–73 is located about 10° longitude westward compared to that derived for the period of 1981–92. Note that this first SVD mode is not very sensitive to the choice of the decadal data if both decades are separated by late 1970s. Note also that the relatively high and low frequencies are alternatively dominant during the former and latter periods. Thus, Fig. 2 suggests that the frequency change may be accompanied by a change of the phase structure between zonal wind stress and SST anomalies. When the zonal wind stress shifts westward (eastward) with respect to the SST anomalies, the corresponding ENSO cycles tend to be of high (low) frequency. This will be examined further in the next section.

To make sure whether the difference shown in Fig. 2 is genuine, an F test is performed. Here, rather than the EOF mode, we compare the composite maps that represent the spatial distribution during the mature phase of each EOF mode. To composite, the magnitudes of the EOF time series that exceeded 1.6 times the standard deviation are selected. Each composite map is almost the same as the original EOF modes shown in Fig. 2 (not shown here). The decadal changes in the dominant wind stress pattern over 170°–130°W are statistically significant at the 95% confidence level. On the other hand, the differences in the SST are not significant.

Although the equatorial zonal distribution of SST anomalies remains almost unchanged during the two different frequency regimes, the subsurface temperature variation has a different story. Figure 3 shows the time–longitude diagram of the equatorial thermocline depth (5°S–5°N) reconstructed using the leading modes obtained from the multichannel singular spectrum analysis (MSSA; Plaut and Vautard 1994; Kim 1996). The thermocline depth is defined by the depth of the 20°C isotherm, which is derived from the NCEP ocean assimilation data from 1980 to 1995 (Ji et al. 1995). Figure 3a shows the sum of the first and second modes, which makes up 64.2% of total variance and is referred to as the low-frequency mode. This mode reflects the major warm and cold events reasonably well. Figure 3b shows the sum of the third and fourth modes, which makes up 12.2% of the total variance and shows a dominant quasi-biannual timescale. This will be referred to as a high-frequency mode. The spatial structures of the low- and high-frequency mode resemble each other in many aspects, such as the standing oscillation pattern between the western and eastern Pacific basins and the propagating feature in the central Pacific. A careful comparison reveals that the positions of the node points of the two modes, which indicate the regions of minimum variability, are quite different. For instance, the node point in the low-frequency mode (Fig. 3a) appears at 165°–145°W, while the node of the high-frequency mode is located between 180° and 160°W. In other words, the zonal position of the nodes of the low-frequency mode is located farther eastward compared to the high-frequency mode. If we calculate the root-mean-square of the thermocline depth anomalies of the low- and high-frequency modes, the zonal shift of the node point can be clearly seen, as shown in Fig. 4. In particular, the

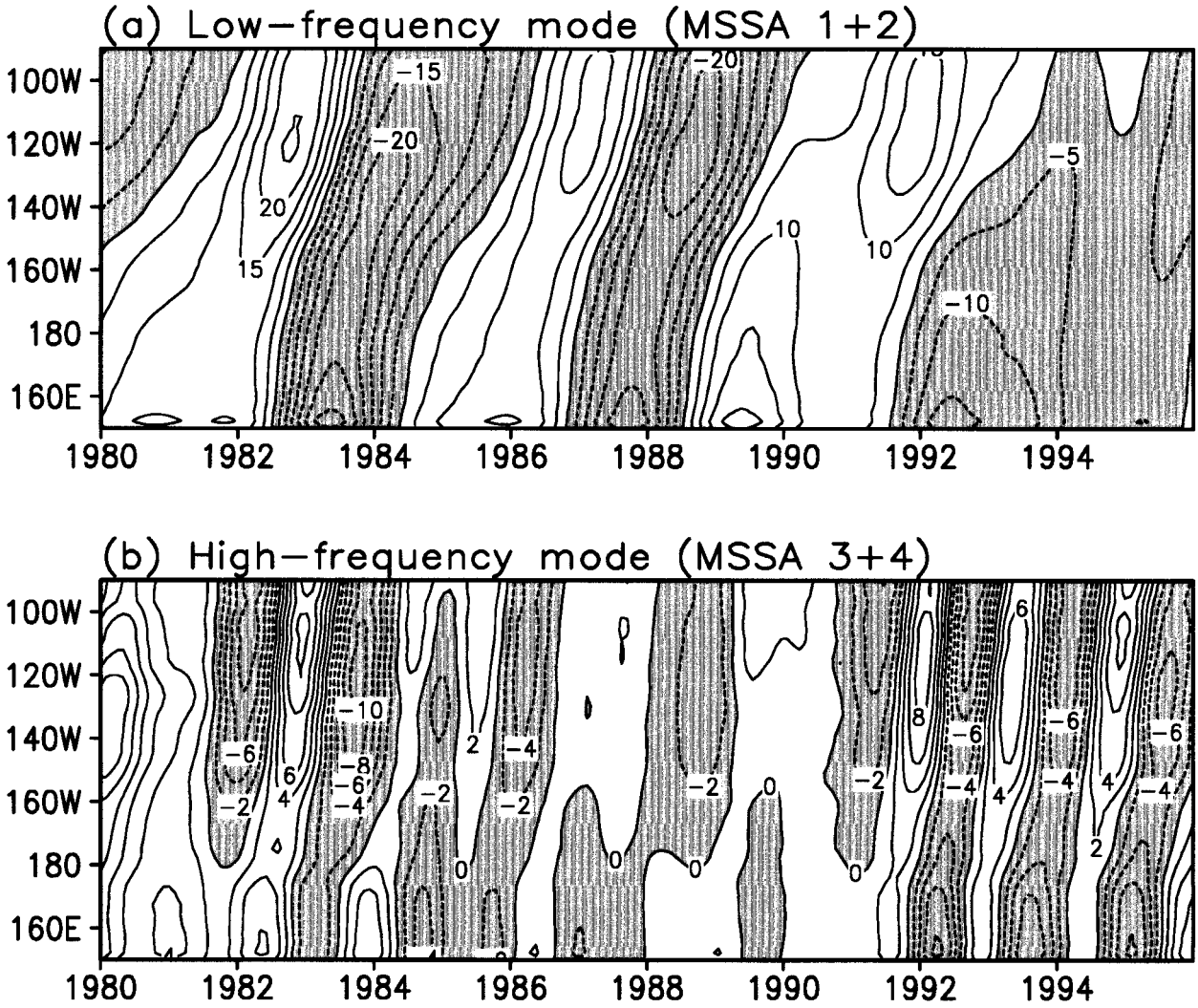

FIG. 3. (a) Low-frequency mode of thermocline depth anomaly (m) averaged over the equatorial region (5°S–5°N). The low-frequency mode is reconstructed by the sum of the first and second MSSA eigenvectors. (b) Same as in (a) but for the high-frequency mode, which is reconstructed by the sum of the third and fourth MSSA eigenvectors.

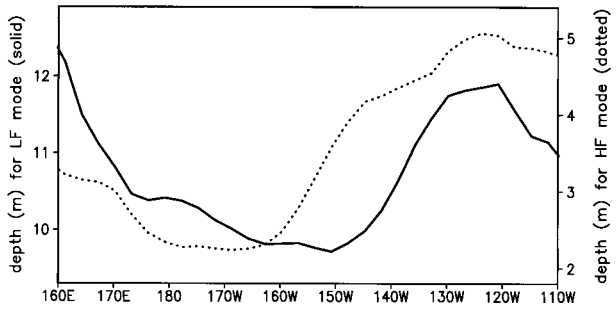

FIG. 4. Longitudinal distribution of the root-mean-square of the equatorial thermocline depth anomaly calculated for the low-frequency (solid) (scale of m on the left side) and high-frequency (dotted) (scale of m on the right side) modes defined in Fig. 3.

difference appeared over 165°–140°W is statistically significant at the 95% confidence level, which is performed by an F test. This difference is consistent with the difference in the longitudinal structure of zonal wind stress for different frequency regimes. This point will be clarified in the next section.

3. Dependence of ENSO frequency on the wind structure: Results of numerical experiments

In the previous section, our data analysis indicates that ENSO frequency varies on an interdecadal timescale. Our analysis also suggests that the zonal structures of the wind stress and thermocline depth vary with ENSO frequency, whereas the zonal structure of SST does not. In this section, we investigate the dynamical connection in the changes between the wind–thermo-

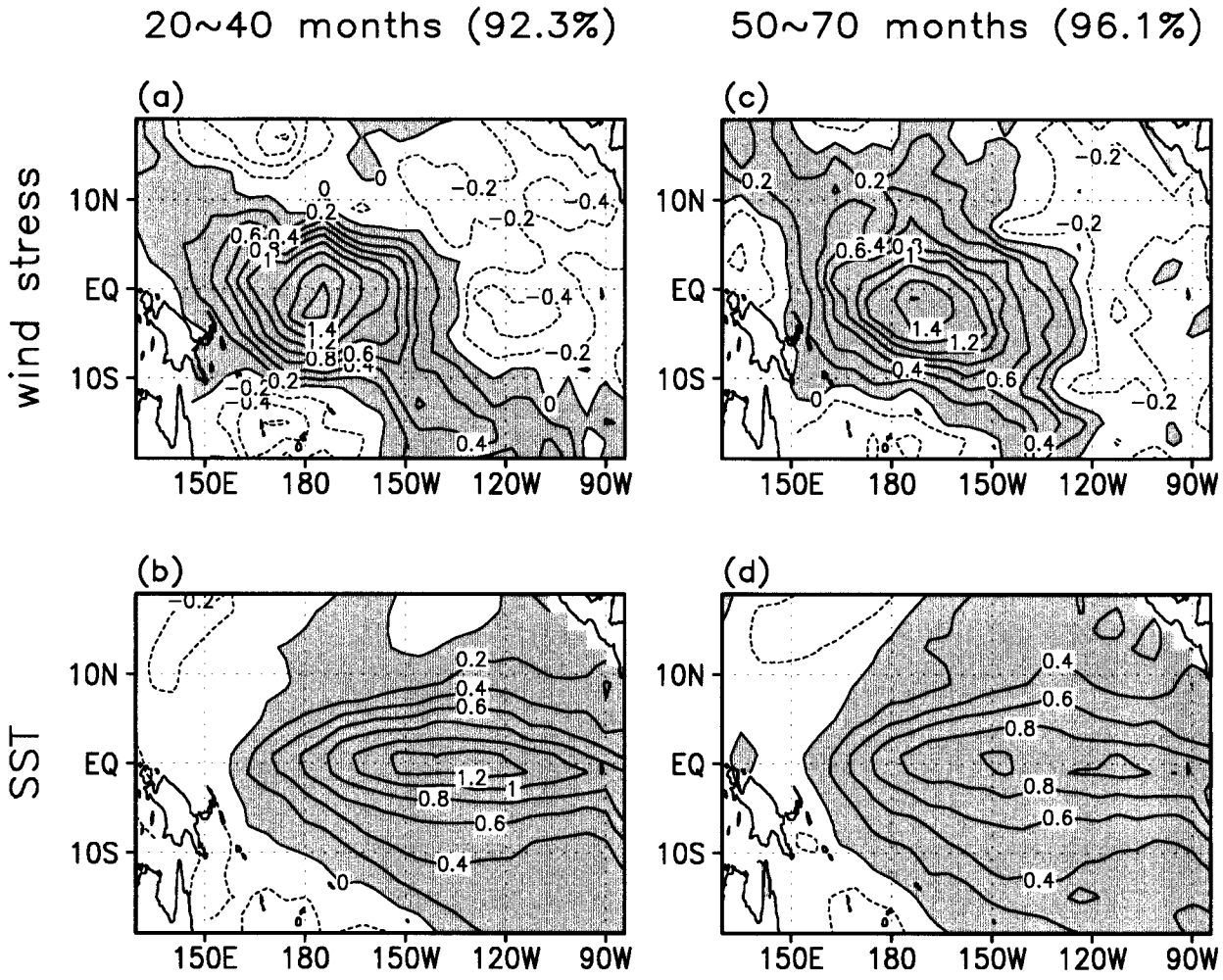

FIG. 5. The first SVD vector of (a) zonal wind stress and (b) SST anomalies derived using the 20–40-month filtered data. (c) and (d) As in (a) and (b) except for the low-frequency mode derived using the 50–70-month filtered data. Units are nondimensional.

cline structure and ENSO frequency. An intermediate coupled ocean–atmosphere model is used to identify the consequences resulting from changes of the spatial structure of ENSO mode. The results demonstrate the importance of the wind stress pattern in determining the ENSO frequency.

The ocean model is basically the same as that used in the Cane–Zebiak (CZ) model (Zebiak and Cane 1987). The atmospheric model is an empirical model describing the linear relationship between observed SST and wind stress anomalies. The empirical atmosphere model is derived using monthly mean SST and wind stress anomalies over the tropical Pacific from January 1963 to December 1993. The SST and wind stress data are obtained from NCEP and FSU, respectively. Using the SVD method, we decompose the monthly mean SST and zonal wind stress anomalies in the forms of Eqs. (1) and (2). We further define a matrix of regression coefficients,

$$C_{mn} = \frac{\langle \alpha_n \beta_m \rangle}{\langle \alpha_n^2 \rangle}, \tag{3}$$

where $\langle\ \rangle$ denotes the time average over the entire length of the sample. Using Eqs. (1)–(3), we can estimate the zonal wind stress anomaly from the SST anomaly. That is,

$$\hat{\tau}_x(x, y, t) = \sum_{m,n} C_{mn} \alpha_n^*(t) f_m(x, y). \tag{4}$$

Here, the value of α_n^* at a given time is calculated by projecting SST anomalies onto the SST eigenvectors e_n. The wind stress field at the given time is calculated by Eq. (4). In the present study, we use only the first SVD mode, which explains over 90% of the total covariance between the SST and zonal wind stress anomalies. Before the decomposition, both the SST and wind stress data are bandpass filtered on two bands of 20–40 and 50–70 months. Consequently, we have two empirical atmosphere models: one is constructed by the high-frequency filtered data (hereafter the HF model) and the other by the low-frequency filtered data (hereafter the LF model).

Figures 5a and 5c show the spatial patterns of the zonal wind stress calculated from the two filtered da-

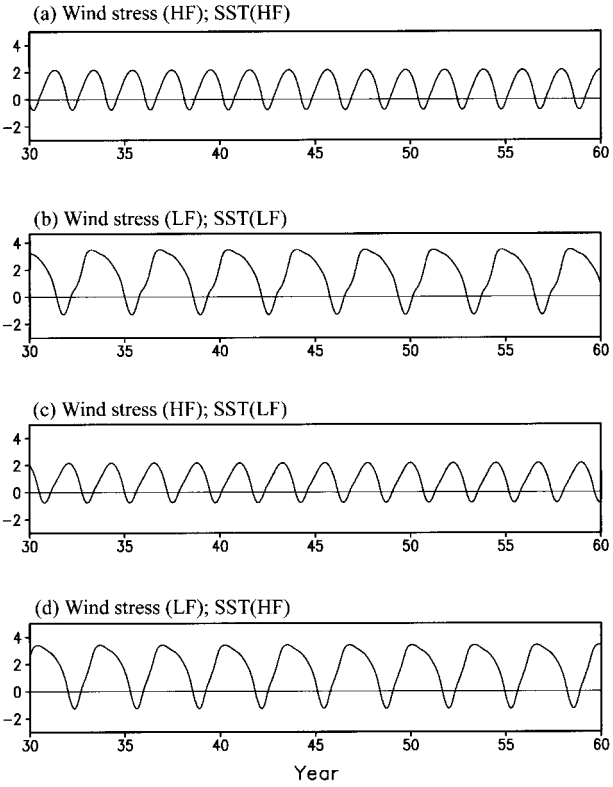

FIG. 6. Time series of Niño-3 SST anomaly calculated by hybrid (empirical atmosphere + Cane–Zebiak ocean) coupled models. The empirical atmosphere is developed by applying the SVD method to 20–40- and 50–70-month filtered data. Units are °C.

tasets. Important differences between the two zonal wind stress patterns associated with the warm phase (shown in Figs. 5a and 5c) are the longitudinal location and meridional extent of the westerly wind anomalies and the strength of the easterly wind stress in the eastern Pacific. The difference between the two filtered anomalous SST fields (Figs. 5b and 5d) are not significant except for the amplitude. The results here thus are consistent with those shown in Fig. 2. Figures 5a and 5b represent the reconstructed HF model and Figs. 5c and 5d the LF model. The two empirical atmosphere models are then coupled with the CZ ocean model. For convenience we simply refer to the two coupled models as the HF and LF models, respectively. In the following experiments, the same annual mean basic states for the ocean and atmosphere are used.

The time series of Niño-3 SST anomaly calculated from the HF model is shown in Fig. 6a. The SST variation in Fig. 6a shows a regular oscillation with a period of 24 months. The Niño-3 SST anomaly obtained from the LF model (Fig. 6b) is a regular oscillation with a period of about 44 months. Both results are qualitatively consistent with their corresponding filtered timescales of the empirical atmospheric models. This suggests that the spatial pattern of the zonal wind stress is responsible for the different oscillation timescales, even though the

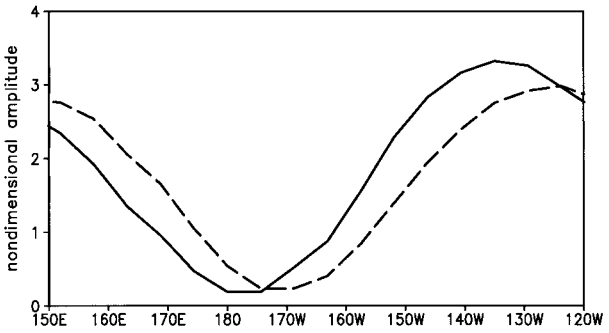

FIG. 7. Longitudinal distribution of the root-mean-square of the MSSA leading eigenvector of oceanic height calculated by the hybrid coupled model. The solid and dashed lines indicate the results derived from the high-frequency (20–40 months) and the low-frequency (50–70 months) models, respectively.

empirical models carry no information about the time evolution of the coupled mode. That means the spatial pattern of the wind stress is indeed critical to the oscillation period of the coupled system.

Considering the fact that there exist some subtle differences in the SST anomalies between the HF and LF models. One may ask whether this is partially the cause for the different oscillation period. In order to check which pattern (SST or wind stress) is important for the modulation of the frequency, we performed two additional experiments. In the first experiment, we construct an artificial empirical atmospheric model, in which the wind stress pattern of the HF model (Fig. 5a) and the SST pattern of the LF model (Fig. 5d) are adopted. In the second experiment, an empirical atmospheric model is formed by using the wind stress pattern of the LF model (Fig. 5c) and the SST pattern of the HF model (Fig. 5b). As shown in Figs. 6c (for the first experiment) and 6d (for the second experiment), the frequency is obviously dependent on the change in the wind stress pattern, not the SST pattern.

To further demonstrate the robustness of the results obtained from the HF and LF models, we examine the subsurface variations in the two models. Figure 7 displays the longitudinal distribution of a *root-mean-square* thermocline depth anomaly derived from the HF and LF models using the first two leading MSSA eigenvectors. The minimum shows the node point in this field. Obviously the zonal distribution of the thermocline depth anomaly in the HF model shifts westward by about 10° longitude compared to that in the LF model. Thus, this zonal phase lag between the thermocline depth simulated by the HF and LF models is also consistent with the observation shown in Fig. 4.

4. Sensitivity of the ENSO frequency to the structure of coupled mode

In the previous section, by using two empirical atmosphere models that are derived from the high- and low-frequency wind–SST anomalies, we showed that

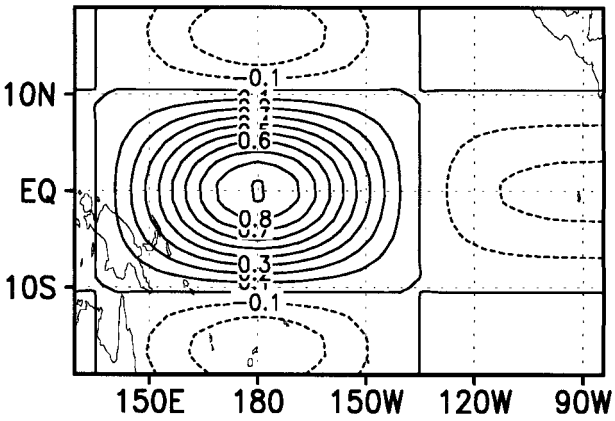

FIG. 8. Spatial pattern of the zonal wind anomalies in the idealized atmospheric model.

TABLE 1. Period (in units of months) and amplitude (in units of °C) of Niño-3 SST anomaly in the sensitivity experiments where the longitudinal position (x_0) of the maximal zonal wind stress shifts from west to east and the meridional *e*-folding scale of wind stress L_y increases.

	X_0			
L_y	160°E	170°E	180°	170°W
7°	11 months 3.5°C	14 months 4.2°C	17 months 4.8°C	25 months 5.3°C
9°	14 months 2.8°C	17 months 4.2°C	24 months 4.9°C	37 months 5.7°C
11°	17 months 1.8°C	20 months 4.3°C	31 months 5.1°C	— 3.2°C
13°	22 months 1.2°C	25 months 4.2°C	— 3.1°C	— 3.2°C

the oscillation period of ENSO is highly dependent upon the spatial pattern of the zonal wind stress. For instance, the spatial patterns of the coupled modes associated with the low- (high-) frequency oscillation during the warm phase of ENSO exhibit an eastward (westward) shift and meridional expansion (compression) of westerly anomalies in the western–central Pacific. In order to show the sensitivity of the ENSO frequency to the spatial structure of the coupled mode, in this section we design an ideal atmosphere model whose spatial structure with respect to a given SST anomaly can be easily changed. The model results may provide information about how the period and amplitude of ENSO cycle respond to the change of structure in wind stress anomalies.

Here, we define an anomalous wind stress pattern whose strength is proportional to the Niño-3 SST anomaly $\mathrm{SSTA}_{\mathrm{NINO3}}$. That is,

$$\tau_x(x, y, t) = \mathrm{SSTA}_{\mathrm{NINO3}}(t)[\Psi_0(y/L_y) - \Psi_2(y/L_y)] \times \left\{\exp\left[-\left(\frac{x - x_0}{L_x}\right)^2\right] - 0.2\right\}, \quad (5)$$

where the horizontal structure is specified on the basis of the empirical wind–SST relationship shown in Figs. 5a and 5c. The functions, ψ_0 and ψ_2 are the zeroth and the second-order Hermite function, respectively; x_0 specifies the longitudinal position of the maximum wind stress; L_x and L_y are the zonal and meridional *e*-folding scales, respectively. Figure 8 shows a spatial pattern of the wind stress calculated using Eq. (5) for the control case where the structure parameters $x_0 = 180°$, $L_x = 35°$, and $L_y = 9°$. Those values are selected so that the resulting wind stress anomaly resembles the spatial pattern derived from observed data shown in Fig. 5a. Thus, in some sense this pattern may be thought of as the leading pattern of the wind stress shown in Fig. 5a. Using Eq. (5), we can also obtain a pattern similar to that in Fig. 5b simply by changing the parameters x_0, L_x, L_y. Moreover, by varying values of x_0 and L_y, we can examine frequency response to changes of the anomalous wind structure in a systematic manner.

The basic states in the following experiments are fixed at the climatological annual mean state. We then shift the zonal wind stress westward or eastward at a 10° interval by changing x_0 and varying the meridional scale L_y from 7° to 13° at a 2° interval. In each case, the coupled model is run for 100 yr. The resulting fluctuations, for example, the time series of Niño-3 SST anomaly, show regular oscillations. The regularity of oscillation is mainly due to the absence of the annual cycle in the basic state, lack of transient (stochastic) forcing, and atmospheric linear response to SST anomalies. However, the frequency and amplitude vary from experiment to experiment. These results are summarized in Table 1.

As shown in Table 1, the control run (with the parameters $x_0 = 180°$ and $L_y = 9°$) produces a 24-month oscillation with an amplitude of 4.9°C. When the maximum westerlies shifts eastward by 10° longitude, the oscillation period increases to 37 months and the amplitude to 5.7°C. On the other hand, when the maximum westerlies shifts 10° westward, the resulting period reduces to 17 months and the amplitude to 4.2°C. In general, the period and amplitude gradually increase when the wind patch shifts eastward. That is consistent with the previous results shown in section 3. Further shifting westward by 30° longitude damps the coupled oscillation, while shifting eastward by 20° longitude brings the coupled system to a permanent warm state. Based on the delayed oscillator paradigm (Suarez and Schopf 1988; Schopf and Suarez 1988; Battisti and Hirst 1989; Cane et al. 1990), we suggest that when the zonal wind anomalies shift far into the eastern Pacific, the negative feedback mechanism is too weak to overcome the positive feedback arising from the coupled instability, leading to a permanent warm state. On the other hand, when the zonal wind anomalies locate too far west, the negative feedback mechanism (e.g., the Ekman upwelling due to the easterly wind anomaly that occupies the wider region including the eastern Pacific) is much stronger

TABLE 2. Period and amplitude of the Niño-3 SST anomaly simulated by the idealized coupled model as a function of the different ratio of the eastern Pacific wind stress. Parameters $X_0 = 180°$, $L_y = 9°$.

	0%	100%	150%	200%
Period (months)	34	24	18	15
Amplitude (°C)	5.8	4.9	4.7	3.9

than the positive feedback due to the coupled instability, thus the oscillation is damped.

Table 1 also indicates that compared to the control run ($L_y = 9°$), when the meridional scale of the westerly anomalies increases by 2° latitude, the oscillation period increases from 24 to 31 months, whereas when L_y reduces by 2° latitude, the period decreases to 17 months. A similar sensitivity test of a CZ-type model to the meridional broadening of the wind stress has been also performed by Kirtman (1997), in which the results are similar to those shown here. This relationship between the period and the meridional scale of the wind stress shown in Table 1 is robust, because it is valid regardless of the position of the zonal wind stress patch. On the other hand, the relationship between the amplitude and the meridional scale of the wind stress depends on the longitudinal location of the maximum westerlies. When the maximum westerlies are located at 170°E, the amplitude does not change appreciably with the meridional scale. If the maximum position moves to 160°E, the amplitude decreases with increasing meridional scales. On the other hand, an eastward shift reverses that relationship. Note also that the amplitude of the permanent warm state is insensitive to the meridional scale and the zonal phase of the zonal wind stress.

As mentioned previously, another difference in the leading SVD modes between the low- and high-frequency regimes (Figs. 5a and 5c) is its amplitude in the tropical eastern Pacific. In order to test the model sensitivities to the wind stress intensity in the eastern Pacific, we vary the strength of the wind stress in the eastern Pacific using Eq. (5). The resulting period and amplitude of the Niño-3 SST anomalies indicate that the period and amplitude almost linearly decrease with increasing intensity of the easterly wind stress during the eastern Pacific warming (Table 2). The effects of the eastern Pacific wind stress in modulation of the amplitude and period of ENSO may be attributed to the changes in local upwelling and the upwelling Kelvin waves generated during the warm event. The latter interfere with the downwelling Kelvin waves generated by the westerly wind stress in the central Pacific. As a result, both effects enhance the negative feedbacks, resulting in a shorter period and a reduced amplitude of ENSO.

As mentioned above, three distinctive differences in the eigenmodes of the zonal wind stress anomaly between the two decades are attributed to the change of ENSO frequency. Among them, the major contributor for change of the period is the zonal shift of the wind fetch, while the change of the meridional scale of the wind stress is a secondary contributor. This can be seen from Table 1. The typical values for x_0 and L_y in Eq. (5), which are associated with the high-frequency epoch, are 180° and 9°, respectively. Those associated with the low-frequency epoch are 170°W and 11°, respectively. The period change due to the zonal shift of wind fetch between the two decades (from 24 to 37 months) is considerably larger than that due to the change of the meridional scale of the wind stress (from 24 to 31 months).

5. Discussion

In the previous sections, we have shown from observation and coupled models that the ENSO period is highly dependent on the zonal phase lag between the wind stress and SST and the meridional scale of wind stress. In this section, we discuss the physical processes that are responsible for the relationships between ENSO frequency and the structure of the coupled mode.

Based on equatorial wave dynamics, the dependence of the period and amplitude of ENSO on the meridional scale of the wind stress anomaly is due to the different adjustment timescales of the thermocline in response to various spatial patterns of the wind stress. For instance, a larger meridional scale of the wind stress favors generation of the higher meridional modes of the ocean Rossby waves, which propagate westward at slower speeds and prolong the timescale of the basinwide thermocline adjustment. As a result, the period is longer. This had been shown by observation (Wang et al. 1999b), a hybrid coupled model (Kirtman and Zebiak 1997), and a theoretical model (Wang and Fang 1996). These also support the delayed oscillator theory, because the higher modes of off-equatorial Rossby waves reduce the negative feedback effects of the equatorial Rossby waves reflected at the western boundary (Kirtman 1997).

Explanation of the dependence of ENSO period on the zonal phase of the wind stress is more complex. One may think a similar argument based on the delayed oscillator theory may work. For instance, if the westerly fetch shifts westward (eastward), the basinwide thermocline adjustment times would be shorter (longer), because the time for Rossby waves reaching western boundary is considerably reduced, although the reflected Kelvin waves may take a slightly longer time to reach the eastern Pacific. The above argument is based only on the effects of thermocline adjustment on ENSO evolution. It is plausible in a qualitative sense but rather ambiguous in a quantitative sense. This is because it does not explain why the adjustment time is so sensitive to a moderate shift in the zonal phase lag between wind stress and SST.

In an effort to provide a quantitative explanation, we analyze the budget for SST tendency. A budget analysis

can reveal important processes responsible for the transition and growth (instability) of ENSO anomalies (e.g., An et al. 1999; Jin and An 1999; Kang et al. 1999, manuscript submitted to *Climate Dyn.*). Among various thermal advection terms that change SST, the vertical advection of subsurface temperature by mean upwelling (referred to as thermocline feedback hereafter) and the zonal advection of the mean SST by anomalous zonal currents (referred to as zonal advection feedback hereafter) have been suggested as major contributors to transition and growth of ENSO (Jin and An 1999; An et al. 1999). Usually, the two feedback mechanisms work together as a result of the quasigeostrophic balance between the zonal currents and the meridional gradients of the thermocline depth. But the relative importance of the two feedback processes to various wind stress patterns may be different. Note that although the advective thermal processes in the CZ model are slightly different from that in the observation (in particular, the vertical heat flux due to the anomalous upwelling), because of the model's simplicity, two important SST budget terms in the coupled model regarded as thermocline and zonal advection feedbacks are consistent with the observation (An et al. 1999; Kang et al. 1999, manuscript submitted to *Climate Dyn.*).

Figure 9 shows the lag covariance between the local SST tendency and the normalized Niño-3 SST anomaly as a function of longitude and the time lag. A positive lag means that the local SST tendency lags Niño-3 SST anomalies. The SST tendency was averaged over 5°S–5°N and the contributions from the thermocline feedback and the zonal advection feedback are presented in the top and bottom panels, respectively. The data used are derived from the numerical experiments performed in section 4 for the different longitudinal locations of the westerly anomalies. Three experiments are compared, in which the positions of maximum westerly, x_0, are located at 170°E, 180°, and 170°W, respectively. The SST tendency in Niño-3 region being in phase with Niño-3 SST anomaly implies an amplification of ENSO anomalies while that being in a quadrature leading Niño-3 SST anomaly indicates a tendency of the transition of ENSO.

In Figs. 9a–c, the positive SST tendencies east of 140°W lead slightly the Niño-3 SST anomaly. This implies that the thermocline feedback favors the transition and growth of ENSO. Interestingly, comparison of Figs. 9a–c indicates that the contribution of the thermocline feedback does not significantly depend on the zonal phase shift of the westerly patch.

In contrast, comparison of Figs. 9d–f indicates that the contribution from zonal advection feedback depends upon the position of the maximum wind stress. The longitudinal areas where SST tendency are in phase (or out of phase) with Niño-3 SST anomaly are very different. For example, when the maximum position of wind stress is at 180° (Fig. 9e), the SST tendency west of 140°W is nearly in phase with the Niño-3 SST anomaly and that east of 140°W leads the Niño-3 SST anomaly with a quarter-cycle. The in phase aspect of SST tendency implies that the zonal advection feedback contributes to growth ENSO, while the leading of SST tendency implies that the zonal advection feedback contributes to transition of ENSO. If the zonal wind stress moves to the west (Fig. 9d), the contribution of the zonal advection feedback to the growth decreases while the contribution to the transition increases. Similarly, when the zonal wind stress shifts eastward (Fig. 9f), the contribution to the growth increases while that to the transition decreases. Therefore, the effects of the zonal advection feedback on ENSO evolution change with the phase shift of the zonal wind stress. In other word, if the zonal wind stress shifts westward, the zonal advection feedback favors transition of ENSO cycle rather than instability (growth); consequently the amplitude decreases and the period becomes shorter as shown in Table 1. Conversely, when the zonal wind stress shifts eastward, the zonal advection feedback favors a longer period and a larger amplitude.

Based on the present results, we can establish a dynamical linkage between the surface response (wind stress and SST anomalies) and the subsurface response (thermocline depth anomaly) associated with the low- and high-frequency regimes. The wind stress during the warm event associated with the low- and high-frequency regimes would be located at the central–eastern Pacific and central–western Pacific, respectively. The responses of thermocline depth to this forcing may resemble those in Figs. 4 or 7. The node point of the thermocline tends to match the longitude separating the region of occupation mostly by Rossby waves and the region of occupation by Kelvin waves, because the zonal pattern of the thermocline on the interannual timescale is characterized by a standing oscillation (Li 1997; An and Kang 2000; Wang et al. 1999b).

In the equatorial region, the anomalous zonal currents, which are maximum in the central Pacific, are generated by the Rossby waves and the local wind stress. Therefore, the zonal currents are very sensitive to the zonal distribution of the wind stress. On the other hand, the thermocline depth in the eastern Pacific is sensitive to the intensity of the local zonal wind. Moreover, the zonal gradients of the mean SST and the mean upwelling are prominent, respectively, in the central Pacific and the eastern Pacific. As a result, the zonal migration of the zonal currents in the central Pacific results in large changes of SST tendency due to the zonal advection of the mean SST by anomalous zonal currents. On the other hand, the small change of the thermocline depth in the eastern Pacific is expected when the zonal wind stress shifts in the central Pacific.

6. Summary and concluding remarks

The period of the ENSO cycle displays an increase in the late 1970s, concurrent with the interdecadal cli-

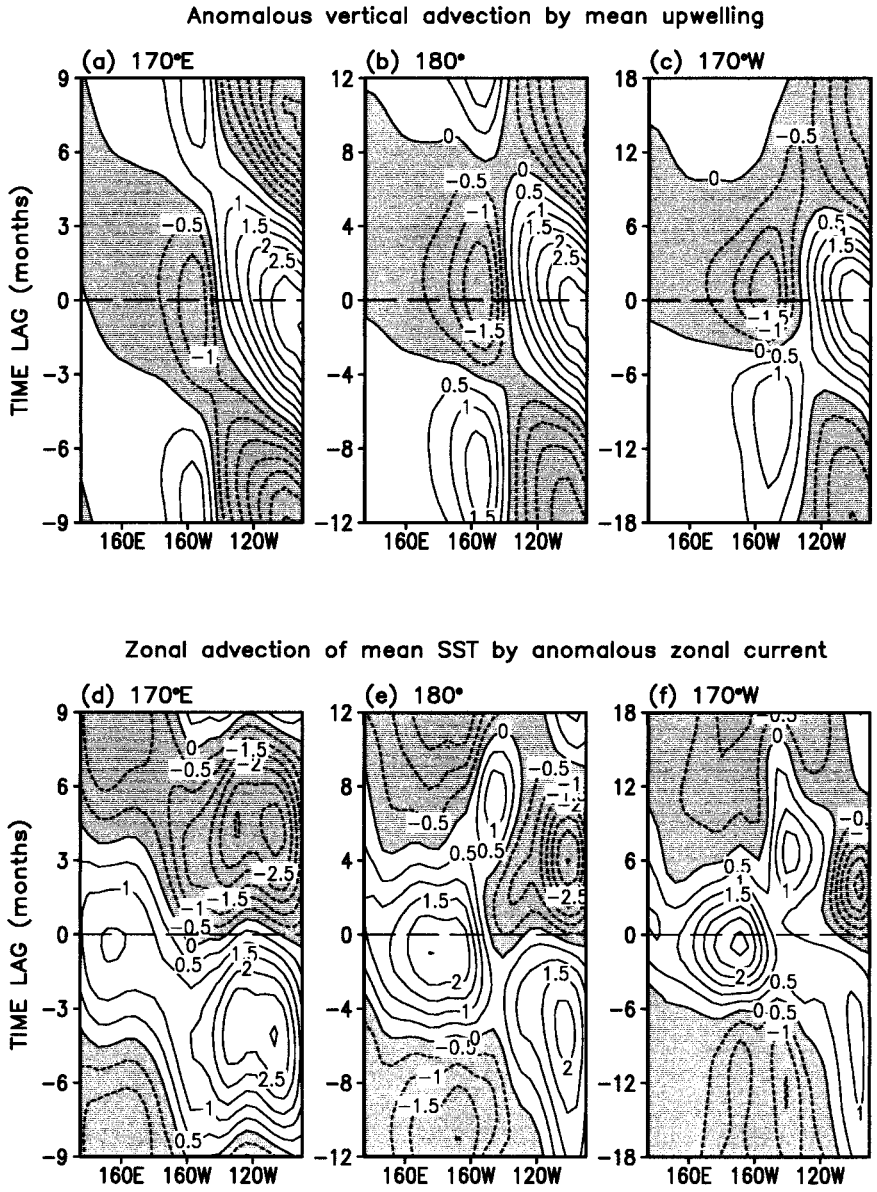

FIG. 9. (a)–(c) Time–longitude section of the lag covariance between the normalized Niño-3 SST anomaly and the local SST tendency due to the advection of subsurface temperature by the mean upwelling. (a), (b), (c) The results derived from the model with maximum westerly located at 170°E, 180°, and 170°W, respectively. (d), (e), (f) The counterparts of (a), (b), and (c), showing the effects of the advection of SST by anomalous zonal currents. Units are 0.1°C month^{-1}.

mate shift in the North Pacific. A high-frequency (period of 20–50 months) and a low-frequency (period of 50–70 months) were dominant for the decade of 1962–73 and the decade of 1981–92, respectively. Observational evidence is presented that suggests that the interdecadal modulation of the ENSO period is closely related to the interdecadal change in the anomalous wind stress distribution in the Tropics, including its zonal phase lag with SST anomalies, the meridional scale, and the intensity in the equatorial eastern Pacific. The equatorial zonal wind stress for the high-frequency decade tends to shift westward compared to that of the low-frequency decade, while SST anomalies for the two decades are essentially the same in terms of the zonal structure. In addition, the equatorial thermocline depth anomaly pattern associated with the high-frequency regime also shifts westward in accord with the westward shift in the zonal wind stress.

In order to confirm the observed linkage between the interdecadal change in the ENSO period and the change in wind stress anomalies, two empirical atmosphere models are developed by applying the SVD method to

the zonal wind stress and SST anomalies filtered for the high- (20–40 months) and low- (50–70 months) frequency bands. These two atmospheric models are then coupled with the same ocean model of Zebiak and Cane (1987). The ENSO period simulated in the coupled model derived from the high-frequency wind–SST relation is much shorter than that derived from the low-frequency counterpart. The zonal phase difference between the thermocline depths simulated by two coupled models is also consistent with observations. The results of these numerical experiments confirm the observed relationship between ENSO frequency and structure.

In comparison with the high-frequency regime, the structure of the coupled mode in the low-frequency regime shows three distinctive features in the zonal wind stress pattern during the warm phase of ENSO: the eastward shift of the westerly anomalies, the meridional expansion of the westerly anomalies in the western–central Pacific, and the weaker intensity of the easterly anomalies in the eastern Pacific. The coupled model experiments using an idealized atmospheric model demonstrate the dependence of the period and amplitude of ENSO on these three factors. For instance, an eastward shift of the maximum westerlies results in a longer period and larger amplitude of ENSO; an expanding meridional scale of wind stress anomalies results in a longer period; an increase of the eastern Pacific wind stress results in a shorter period and a smaller amplitude. Among them, the zonal shift of the wind stress anomaly turned out to be the primary factor contributing to the change of ENSO frequency.

The ENSO period change due to the broadening of the meridional scale in the zonal wind stress anomalies is argued to be related to the change of the thermocline adjustment time. The broadening of the meridional scale in the wind stress anomalies favors generation of the higher meridional modes of Rossby waves and leads to a slower basinwide thermocline adjustment and a longer oscillation period. The dramatic increase of period due to a moderate eastward shift of wind stress, however, cannot be quantitatively explained by the time delay for Rossby waves reaching the western boundary. Our temperature tendency diagnostics suggest that the zonal shift of the wind stress anomalies affects ENSO evolution through advection of the mean SST by anomalous zonal currents. Through this zonal advection feedback, the eastward shift of the wind stress anomalies enhances the growth of coupled mode and delays the transition of the ENSO cycles, thus resulting in a larger amplitude and a longer period. The SST tendency analysis clarifies not only the mechanism related to the period change but also that of the amplitude change.

The conventional wisdom suggests that the intensity of the ocean–atmosphere coupling is important to determine not only the amplitude but also the frequency of ENSO. To a certain degree, the frequency of the linear coupled system depends on coupling coefficients (Hirst 1986, 1988; Wakata and Sarachik 1991; Jin and Neelin 1993). Then, how sensitive is the ENSO frequency to the coupling coefficient in the nonlinear CZ model? We found that the dominant period of oscillation only weakly depends on the coupling coefficient (Table 3). The period for the original coupling coefficient is about 48 months. When the coupling coefficient is either increased or decreased by 20% of the original value, the period does not change much (from 45 to 48 months). On the other hand, the hybrid model used in section 4 for the basic state including annual cycle displays a dramatic change of the ENSO period in response to even a moderate zonal shift of the wind stress. For example, an eastward shift of the westerly wind anomalies by 20° results in an increase in oscillation period by 1 yr, while a 10° shift westward makes the ENSO period one year shorter. These experiments seem to indicate that the ENSO period in the CZ model is much more sensitive to the spatial structure of wind stress than to the coupling coefficient.

TABLE 3. Period simulated by the CZ model with various coupling coefficients. Basic states include annual cycles.

Coupling coefficient	0.8	1.0	1.2	1.4	1.8
Period (months)	~48	~48	~45	~43	~43

In the contrast to our mechanism, Kirtman and Schopf (1998) found that the change of ENSO frequency could be related to whether the delayed oscillator mechanism is controlling the variability or not, without a change in the structure of the ENSO mode. However, the observation strongly suggests the significant change in the structure of the coupled ENSO mode between the two decades. Although we found that the change of ENSO frequency is accompanied by the change of the structure of ENSO mode and demonstrated that the change of structure can affect the frequency, we did not address the important question of what actually causes the change in the spatial pattern of wind anomalies during the two decades. Here, we speculate that the change of basic state on the interdecadal timescale may have contributed to the changes in the spatial structure of ENSO modes. Our current research is exploring this possibility and the results will be reported.

Acknowledgments. The authors appreciate the comments made by Dr. Ben Kirtman and an anonymous reviewer. Thanks are extended to Diane Henderson for her careful edit of the manuscript. Soon-Il An has been supported by Frontier Research System for Global Change. Bin Wang acknowledges support from OGP/NOAA through GOALS and PACS programs.

REFERENCES

An, S.-I., and I.-S. Kang, 2000: A further investigation of the recharge oscillation paradigm for ENSO using a simple coupled model

with the zonal mean and eddy separated. *J. Climate,* **13,** 1987–1993.
——, F.-F. Jin, and I.-S. Kang, 1999: The role of zonal advection feedback in phase transition and growth of ENSO in the Cane-Zebiak model. *J. Meteor. Soc. Japan,* **77,** 1151–1160.
Balmaseda, M. A., K. Davey, and D. L. T. Anderson, 1995: Decadal and seasonal dependence of ENSO prediction skill. *J. Climate,* **8,** 2705–2715.
Barnett, T. P., D. W. Pierce, M. Latif, and D. Dommenget, 1999: Interdecadal interactions between the tropics and midlatitudes in the Pacific basin. *Geophys. Res. Lett.,* **26,** 615–618.
Battisti, S. D., and A. C. Hirst, 1989: Interannual variability in the tropical atmosphere–ocean model: Influence of the basic state, ocean geometry, and nonlinearity. *J. Atmos. Sci.,* **46,** 1687–1712.
Bretherton, C. S., C. Smith, and J. M. Wallace, 1992: An intercomparison of methods for finding coupled patterns in climate data. *J. Climate,* **5,** 541–560.
Cane, M. A., M. Munnich, and S. E. Zebiak, 1990: A study of self-excited oscillations of the tropical ocean–atmosphere system. Part I: Linear analysis. *J. Atmos. Sci.,* **47,** 1562–1577.
Goldenberg, S., and J. O'Brien, 1981: Time and space variability of the tropical Pacific wind stress. *Mon. Wea. Rev.,* **109,** 1190–1207.
Gu, D., and S. G. H. Philander, 1997: Interdecadal climate fluctuations that depend on exchanges between the tropics and extratropics. *Science,* **275,** 805–807.
Hirst, A. C., 1986: Unstable and damped equatorial modes in simple coupled ocean–atmosphere models. *J. Atmos. Sci.,* **43,** 606–630.
——, 1988: Slow instabilities in tropical ocean basin–global atmosphere models. *J. Atmos. Sci.,* **45,** 830–852.
Ji, M., A. Leetmaa, and J. Derber, 1995: An ocean analysis system for seasonal to interannual climate studies. *Mon. Wea. Rev.,* **123,** 460–481.
Jin, F.-F., and J. D. Neelin, 1993: Modes of interannual tropical ocean–atmosphere interaction—A unified view. Part I: Numerical results. *J. Atmos. Sci.,* **50,** 3477–3503.
——, and S.-I. An, 1999: Thermocline and zonal advective feedbacks within the equatorial ocean recharge oscillator model for ENSO. *Geophys. Res. Lett.,* **26,** 2989–2992.
Kim, K.-M., 1996: Temporal and spatial structures of the seasonal and interannual variability of the tropical Pacific atmosphere and ocean. Ph.D. thesis, Seoul National University, 135 pp. [Available from Department of Atmospheric Sciences, Seoul National University, Seoul 151-742, Korea.]
Kirtman, B. P., 1997: Oceanic Rossby wave dynamics and the ENSO period in a coupled model. *J. Climate,* **10,** 1690–1704.
——, and S. E. Zebiak, 1997: ENSO simulation and prediction with a hybrid coupled model. *Mon. Wea. Rev.,* **125,** 2620–2641.
——, and P. S. Schopf, 1998: Decadal variability in ENSO predictability and prediction. *J. Climate,* **11,** 2804–2822.
Kubota, M., and J. J. O'Brien, 1988: Variability of the upper tropical Pacific Ocean model. *J. Geophys. Res.,* **93,** 7155–7166.
Kushnir, Y., 1994: Interdecadal variations in North Atlantic sea surface temperature and associated atmosphere conditions. *J. Climate,* **7,** 141–157.
Latif, M., and T. P. Barnett, 1994: Causes of decadal climate variability over the North Pacific and North America sector. *Science,* **266,** 634–637.
Lau, K.-M., and H. Weng, 1995: Climate signal detection using wavelet transform: How to make a time series sing. *Bull. Amer. Meteor. Soc.,* **76,** 2391–2402.
Li, T., 1997: On the phase transition of the El Nino–Southern Oscillation: A stationary SST mode. *J. Atmos. Sci.,* **54,** 2872–2887.
Meyers, S. D., B. G. Kelly, and J. J. O'Brien, 1993: An introduction to wavelet analysis in oceanography and meteorology: With application to the dispersion of Yanai waves. *Mon. Wea. Rev.,* **121,** 2858–2866.
Nitta, T., and S. Yamada, 1989: Recent warming of tropical sea surface temperature and its relationship to the Northern Hemisphere circulation. *J. Meteor. Soc. Japan,* **67,** 375–383.
Plaut, G., and R. Vautard, 1994: Spells of low-frequency oscillations and weather regimes in the Northern Hemisphere. *J. Atmos. Sci.,* **51,** 210–236.
Reynolds, R. W., and T. M. Smith, 1994: Improved global sea surface temperature analysis using optimum interpolation. *J. Climate,* **7,** 929–948.
——, and ——, 1995: A high resolution global sea surface temperature climatology. *J. Climate,* **8,** 1571–1583.
Schopf, P. S., and M. J. Suarez, 1988: Vacillations in a coupled atmosphere–ocean model. *J. Atmos. Sci.,* **45,** 549–566.
Shriver, J. F., and J. J. O'Brien, 1995: Low-frequency variability of the equatorial Pacific ocean using a new pseudostress dataset: 1930–1989. *J. Climate,* **8,** 2762–2786.
Smith, S. R., C. Harvey, and D. M. Legler 1996: Handbook of quality control procedures and methods for surface meteorology data. Data Assembly Center for Surface Meteorology, Center for Ocean Atmospheric Prediction Studies Tech. Rep. 96-1, 56 pp. [Available from The Florida State University, Tallahassee, FL 32306-3041.]
Smith, T. M., R. W. Reynolds, and C. F. Ropelewski, 1994: Optimal averaging of seasonal sea surface temperatures and associated confidence intervals (1860–1989). *J. Climate,* **7,** 949–964.
——, ——, R. E. Livezey, and D. C. Stokes, 1996: Reconstruction of historical sea surface temperature using empirical orthogonal functions. *J. Climate,* **9,** 1403–1420.
Suarez, M. J., and P. S. Schopf, 1988: A delayed oscillator for ENSO. *J. Atmos. Sci.,* **45,** 3283–3287.
Trenberth, K. E., 1990: Recent observed interdecadal climate changes in the Northern Hemisphere. *Bull. Amer. Meteor. Soc.,* **71,** 988–993.
——, and J. W. Hurrel, 1994: Decadal atmosphere–ocean variations in the Pacific. *Climate. Dyn.,* **9,** 303–319.
Wakata, Y., and E. S. Sarachik, 1991: Unstable coupled atmosphere-ocean basin modes in the presence of a spatially varying basic state. *J. Atmos. Sci.,* **48,** 2060–2077.
Wang, B., 1995: Interdecadal changes in El Nino onset in the last four decades. *J. Climate,* **8,** 267–285.
——, and Z. Fang, 1996: Chaotic oscillations of tropical climate: A dynamic system theory for ENSO. *J. Atmos. Sci.,* **53,** 2786–2802.
——, and Y. Wang, 1996: Temporal structure of the Southern Oscillation as revealed by waveform and wavelet analysis. *J. Climate,* **9,** 1586–1598.
——, A. Barcilon, and Z. Fang, 1999a: Stochastic dynamics of El Niño–Southern Oscillation. *J. Atmos. Sci.,* **56,** 5–23.
——, R. Wu, and R. Lukas, 1999b: Roles of the western North Pacific wind variation in thermocline adjustment and ENSO phase transition. *J. Meteor. Soc. Japan,* **77,** 1–16.
Zebiak, S. E., and M. A. Cane, 1987: A model El Niño–Southern Oscillation. *Mon. Wea. Rev.,* **115,** 2262–2278.
Zhang, R.-H., and S. Levitus, 1997: Structure and cycle of decadal variability of upper ocean temperature in the North Pacific. *J. Climate,* **10,** 710–727.
——, L. M. Rothstein, and A. J. Busalacchi, 1998: Origin of upper ocean warming and El Niño change on decadal scales in the tropical Pacific Ocean. *Nature,* **391,** 879–883.